PAPER

Embedded 3D printing of engineered lung cancer model for assisting fine-needle aspiration biopsy

To cite this article: Weijian Hua *et al* 2025 *Biofabrication* **17** 015042

Biofabrication

PAPER

Embedded 3D printing of engineered lung cancer model for assisting fine-needle aspiration biopsy

Weijian Hua[1], Cheng Zhang[1,2], Lily Raymond[1], Kellen Mitchell[1], Kuo Xiao[3], Ryan Coulter[1], Erick Bandala[1], Manish Bishwokarma[4], Ying Yang[4,*], Danyang Zhao[2,*], Na Xiao[5,*] and Yifei Jin[1,*]

[1] Department of Mechanical Engineering, University of Nevada, Reno, Reno, NV, United States of America
[2] State Key Laboratory of High-Performance Precision Manufacturing, School of Mechanical Engineering, Dalian University of Technology, Dalian, Liaoning, People's Republic of China
[3] Department of Thoracic Surgery, Affiliated Hospital of Hebei University, Baoding, Hebei, People's Republic of China
[4] Department of Chemistry, University of Nevada, Reno, Reno, NV, United States of America
[5] Department of Medical Oncology, Affiliated Hospital of Hebei University, Baoding, Hebei, People's Republic of China
[*] Authors to whom any correspondence should be addressed.

E-mail: yingy@unr.edu, zhaody@dlut.edu.cn, 15832225218@163.com and yifeij@unr.edu

Keywords: embedded 3D printing, respiratory tract-blood vessel system, yield-stress fluid, lung cancer, fine-needle aspiration biopsy

Supplementary material for this article is available online

RECEIVED
30 June 2024

REVISED
1 December 2024

ACCEPTED FOR PUBLICATION
16 December 2024

PUBLISHED
30 December 2024

Abstract

Lung cancer is a serious global health issue that requires the development of patient-specific, lung cancer model for surgical planning to train interventionalists and improve the accuracy of biopsies. Although the emergence of three-dimensional (3D) printing provides a promising solution to create customized models with complicated architectures, current 3D printing methods cannot accurately duplicate anatomical-level lung constructs with tumor(s) which are applicable for hands-on training and procedure planning. To address this issue, an embedded printing strategy is proposed to create respiratory bronchioles, blood vessels, and tumors in a photocurable yield-stress matrix bath. After crosslinking, a patient-specific lung cancer analogous model is produced, which has tunable transparency and mechanical properties to mimic lung parenchyma. This engineered model not only enables the practical training of fine-needle aspiration biopsy but also provides the necessary information, such as coordinates of aspiration, wound depth, and interference with surrounding tissues, for procedure optimization.

1. Introduction

Lung cancer is one of the most common diseases among human beings and has become the leading cause of mortality globally [1–3]. A biopsy is a crucial step in lung cancer diagnosis and therapy, which provides essential information to guide the treatment decisions in different stages and/or categories of lung cancer [4–6].

Among diverse biopsy strategies, fine-needle aspiration (FNA) biopsy is of great significance and popularity because of its exceptional advantages, such as minimal trauma, quick procedure, low cost, rapid diagnosis, etc [7–9]. In FNA biopsy, a thin, hollow needle is inserted through the patient's chest wall to reach the lung tumor, which directly samples living cells for examination under a microscope. During this process, some imaging methods, like computed tomography (CT) and endobronchial ultrasound (EBUS), are required to guide the needle to accurately target the tumor [10–12]. Although both CT- and EBUS-guided FNA biopsies are efficient methods for diagnosing lung cancer, the accuracy and success of the procedure are highly dependent on the skill and experience of interventionalists who perform the biopsies [13, 14]. Therefore, it is necessary to develop a patient-specific, *in vitro* lung cancer analogous model to make interventionalists well-trained and prepared before the procedure.

The emergence of three-dimensional (3D) printing technology provides a promising tool to create customized models with complicated architectures [15–17]. Although in FNA biopsy 3D printing is predominantly applied to produce individualized guide plates [18–20], various approaches are still utilized specifically for lung cancer-relevant applications. For

example, Mei *et al* [21] used the digital light processing technique to generate a perfusable 3D lung cancer model. In their work, cancer cells were mixed with gelatin methacrylate (GelMA) and printed into 0.75 mm thick layers to function as a small-sized 3D cancer model for drug screening. Herreros-Pomares *et al* [22] applied another light-based 3D bioprinting technique, stereolithography (SLA), to construct GelMA-polyethylene glycol diacrylate (PEGDA) scaffolds for culturing lung cancer stem cells. These studies mainly focused on unveiling cancer cell behaviors based on 3D printed models with simple architectures, failing to serve for procedure planning and interventionalist training. For the reconstruction of anatomical-level lung cancer models, Liu *et al* [23] applied SLA to fabricate a sophisticated lung model from photocurable resin. This model was composed of nodules, bronchi, and pulmonary vessels. However, the mechanical properties of this model cannot match with those of human lung tissues. Therefore, the model was only used for qualitatively assessing the pulmonary vessel and bronchi branching patterns in surgery planning. It has not been applied to offer either quantitative data for further optimizing the procedure or hands-on opportunities for surgery training. Yoon *et al* [24] developed a hybrid printing-casting method to make a personalized model for informed consent for stage I lung cancer. In this method, fused deposition modeling (FDM), a popular material extrusion-based 3D printing approach, was utilized to fabricate the trachea and bronchial tree which was subsequently encapsulated by transparent resin through casting. The main purpose of this model was to more effectively convey a personalized explanation to patients about the surgical plan, rather than for hands-on training applications. Similarly, Baba *et al* [25] printed a thyroid gland model from the commercial acrylic resin. Since its mechanical properties were far away from those of human tissues, the primary purpose of this model was educational. In summary, current 3D printing methods cannot accurately duplicate anatomical-level lung constructs with tumor(s) which are applicable for hands-on training and planning for interventionalists before the procedure. Therefore, it calls for the development and innovation of more effective printing processes.

The focus of this work is to use embedded 3D printing to fabricate an engineered lung cancer model which not only reproduces the complicated architectures of human lungs with tumors, but also possesses matching biomechanical properties for training FNA biopsy operations. In this model, respiratory bronchioles, blood vessels, and tumors are created in a photocurable yield-stress matrix bath with tunable transparency and mechanical properties to mimic lung parenchyma. In order to improve the printing efficiency, a new path design strategy is developed to generate the printing path of each vessel as well as the printing sequence of the vessels. After crosslinking, a patient-specific lung cancer analogous model is produced, which enables the practical training of FNA. Additional, necessary information, such as coordinates of aspiration, wound depth, and interference with surrounding tissues, can be obtained to further optimize the procedure. This model functions as a reliable tool for enhancing lung cancer diagnosis and therapy.

2. Materials and methods

2.1. Material preparation

For the photocurable yield-stress matrix bath, a nanoclay-Pluronic F127-PEGDA nanocomposite was developed and prepared per the following protocol. A stock solution of PEGDA (Mn 700, Sigma-Aldrich, St. Louis, MO) was diluted with deionized (DI) water at room temperature. Then, the photoinitiator (2-hydroxy-4′-(2-hydroxyethoxy)-2-methylpropiophenone, Sigma-Aldrich, St. Louis, MO) was added to the diluted PEGDA solution and thoroughly mixed using an overhead stirrer (LACHOI, Shaoxing, China) at 800 rpm for at least 10 min. After that, an appropriate amount of Laponite® RD powder (BYK Additives Inc., Gonzales, TX) was dispersed into the PEGDA solution at room temperature and continuously stirred using the overhead stirrer (800 rpm) until the nanoclay powder was fully hydrated. Finally, an appropriate amount of Pluronic F127 powder (P2443, Sigma-Aldrich, Burlington, MA) was added to the nanoclay-PEGDA suspension and mixed by the stirrer (1000 rpm) at 4 °C until the nanocomposite was clear and homogeneous. To investigate the effects of nanocomposite formula on rheological properties, transparency, and mechanical properties, the PEGDA concentration was varied at 10%, 15%, and 20% (v/v), the photoinitiator concentration was changed from 0.2% to 0.5%, and 0.8% (w/v), the nanoclay concentration was tuned at 1%, 2%, and 3% (w/v), and Pluronic F127 was added at 10, 15, and 20% (w/v). After preparation, all nanocomposites were degrassed using a centrifuge (Cole-Parmer® VS3400, Cole Parmer Instrument Company, Vernon Hills, IL) at 3000 rpm for 2 min to remove entrapped air bubbles and then stored in sealed containers at 4 °C for one-day aging before use.

A commercial clear epoxy resin (EcoPoxy Inc., Manitoba, Canada) was selected to print the respiratory bronchioles, blood vessels, and tumors within the photocurable yield-stress matrix bath. Based on the manufacturer's protocol, the epoxy-based ink was prepared by uniformly mixing parts A and B at the volume ratio of 1:1. For improving the printability of the epoxy-based ink, fumed silica (Aerosil R812, Evonik, Parsippany, NJ) was mixed in the pure epoxy

base at 6% (w/v) by the overhead stirrer (600 rpm for 20 min). To distinguish different structures, a dye (RIT, Nakoma Products LLC, IL) was added to the epoxy mixture at 0.5% (v/v). Specifically, the red, black, yellow, and ochre dyes were used to demonstrate the printed arteries, veins, tracheae, and tumor, respectively.

2.2. Measurements of rheological properties

The rheological properties of the nanocomposites and epoxy ink were measured using a rotational rheometer (MCR 92, Anton Paar USA Inc., Ashland, VA) equipped with a cone-plate measuring system (angle: 1°, diameter: 50 mm, and cone-to-plate gap distance: 0.102 mm). The oscillatory tests were employed to quantify the yield stress values of the nanocomposite samples, which were subjected to the shear stress varying from 1 to 1000 Pa at a constant frequency of 1 Hz. The shear moduli were recorded. The yield stress value of each sample was determined from the point of intersection between the storage modulus and loss modulus on the shear moduli-shear stress curve. After that, the three-interval thixotropy tests were applied to the nanocomposite with 3% (w/v) nanoclay, 20% (w/v) Pluronic F127, 20% (v/v) PEGDA, and 0.2% (w/v) photoinitiator to test its recovery capability at room temperature. In the first interval, the nanocomposite was subjected to the shear rate of 0.1 s^{-1} for 100 s. In the second interval, the shear rate was increased to 100 s^{-1} for 20 s. In the third interval, the shear rate was reverted to 0.1 s^{-1} for 100 s. The viscosity variation was recorded during this process. Then, the dynamic time sweeps were conducted on the same nanocomposite at room temperature with a frequency of 1 Hz. The purpose was to characterize the reversibility of the nanocomposite when serving as a yield-stress matrix bath. In the sweeps, the nanocomposite was sheared at the strain of 1% for 300 s. Then, the strain was increased to 100% for another 300 s. These processes were repeated for 1500 s totally to record the storage and loss moduli in response to strain variation. Finally, the steady shear rate sweeps were performed on the pure epoxy and fumed silica-epoxy mixture at room temperature with the shear rate increasing from 1 to 1000 s^{-1}. The shear stress at each shear rate was measured. Based on the Herschel–Bulkley model [26], the yield stress values were calculated.

2.3. Characterization of transparency

To characterize the transparency of the nanocomposites with different formulas, the specimens were prepared by pouring the given volume of nanocomposites into the Petri dishes (Acrylic jars, Beauticom Inc., CA) and crosslinked using an ultraviolet (UV) curing system (OmniCure Series 2000, wavelength: 320–500 nm, Lumen Dynamics, Mississauga, Canada). The exposure time was 10 min. After UV crosslinking, the specimens with a diameter of 27 mm and thickness of 6 mm were placed on a high-precision measurement system (VERTEX 251UC, Micro-Vu, Windsor, CA) to take photos. The ImageJ software (https://imagej.nih.gov/ij/) was applied to analyze the brightness. By contrasting the brightness of nanocomposite specimens (B_n) to that of the clear Petri dish (B_0), the transparency ratio was characterized by the following equation:

$$\text{Transparency ratio} = \frac{B_n}{B_0}.$$

2.4. Measurements of mechanical properties

The mechanical properties of the nanocomposites after UV crosslinking were measured at room temperature using a mechanical tester (AGS-X, Shimadzu Corporation, Kyoto, Japan). The uniaxial compression tests were performed on the nanocomposite specimens, which were prepared by filling the nanocomposites into the homemade cylindrical polydimethylsiloxane molds (Φ13.0 mm × 9.0 mm) and crosslinking via the UV curing system. The specimens were then released from the molds and loaded to the mechanical tester for compression at a strain rate of 1 mm min^{-1}. The force and displacement data were recorded to plot the stress–strain curves based on the specimen geometries. The elastic modulus of each nanocomposite specimen was determined from the slope of the corresponding curve.

2.5. Filament printing and characterization

A homemade embedded ink writing system was utilized to print filaments from the epoxy-based ink at different path speeds, which was modified based on an FDM 3D printer (SOVOL 3D, Shenzhen Liandian Technology Co., Ltd, Shenzhen, China). The printing conditions were summarized as follows: dispensing nozzle of 14-gauge (inner diameter of 1.52 mm and length of 25.4 mm, EFD Nordson, Vilters, Switzerland) and dispensing pressure of 10 psi (0.7×10^5 Pa). The filaments were printed at two path speed ranges (i.e. from 2 to 100 mm s^{-1} and from 2 to 8 mm s^{-1}) to investigate the effects of path speed on filament diameter as well as to determine the suitable speeds for printing respiratory bronchioles and blood vessels. To improve the visibility, the red dye was added to the epoxy ink at 0.5% (v/v). A camera (120fps USB Camera, ELP, Shenzhen, China) was applied to record the filament formation process and filament diffusion in the matrix bath over time (24 h). The dimensions in the filament images were measured using ImageJ.

For making the tumor model, the same nozzle was used to deposit the epoxy-based ink at zero path speed. The same dispensing pressure was applied for different time durations (1–10 s) to generate spherical

tumors with varying diameters, which were recorded by the camera and measured by ImageJ.

2.6. Path generation

A healthy lung model was directly downloaded from a website (www.3d66.com/). After confirming with the clinicians at the Affiliated Hospital of Hebei University, a tumor model with an overall size of 6.0 mm in diameter was integrated with the lung model as the patient-specific lung cancer model. To save the fabrication time, only a portion of the model was extracted for printing which had a length of 46.0 mm, width of 46.0 mm, and height of 22.0 mm. This portion possessed all necessary components (i.e. arteries, veins, tracheae, and tumors) to represent the whole lung cancer model. To generate the printing trajectory of each component, the lung cancer model constructed using SolidWorks 2023 (Dassault Systemes SolidWorks Corp., Waltham, MA) was first exported as an STL file. This file was then imported into Rhino 8 (trial version available from www.rhino3d.com/), where the model was converted into a NURBS surface. Using the Grasshopper plugin within Rhino 8, the model was divided into a uniform lattice structure with a side length of 1.0 mm. The Crystallon plugin was then employed to merge the lattice lines into a single path that described the model's printing paths.

Subsequently, a customized Python script was used to sequentially export the spatial coordinates of the path segment endpoints into a CSV file. An edge validation algorithm, developed in-house using MATLAB (The MathWorks Inc., Natick, MA), was then applied to determine if the line segments forming the path interfered with one another. Finally, interference-free segments were used to generate printable paths according to a path planning algorithm developed in MATLAB, and exported as G-code commands suitable for execution by 3D printers.

2.7. Lung cancer model printing and characterization

The homemade embedded ink writing system was applied to reconstruct the selected portion of the lung cancer model using the 14-gauge nozzle and dispensing pressure of 10 psi. For the arteries, the path speed was continuously adjusted at 4 and 7 mm s^{-1} to achieve the vessel diameters of 3.73 and 2.74 mm, respectively, based on the generated printing trajectories. For the veins, the path speed was controlled at 5 and 8 mm s^{-1} to make the vessel diameters equal to 3.33 and 2.44 mm, respectively. For the tracheae, the path speed was changed to 3 and 4 mm s^{-1} during printing to obtain the filament sizes of 4.38 and 3.73 mm, respectively. For the tumor, the nozzle was moved to the corresponding coordinates without depositing inks and extruding the epoxy-based ink at the coordinates for 3 s. After embedded printing, the matrix bath with different components was exposed to UV radiation for 20 min to crosslink the nanocomposite and then kept at room temperature for 24 h to crosslink the components from the epoxy-based ink. To evaluate the accuracy of printed results, OpenCV and scikit-image were called from Python libraries to calculate the structural similarity index measure (SSIM) between the designed and printed models.

Three datum planes from polylactic acid (EP e36, Shenzhen Creality 3D Technology Co, Ltd, Shenzhen, China) were printed using an FDM 3D printer (SOVOL 3D, Shenzhen Liandian Technology Co., Ltd, Shenzhen, China) and integrated with the lung cancer model. A homemade inserting device was established to punch a fine needle (0.3 mm in diameter, Uxcell, China) into the model at different locations. An angle finder (Hyper Tough^{TM}, Walmart Inc., AR) was used to measure the angles of the needle projected into different datum planes. Additionally, the insertion depths at different locations were also characterized by measuring the needle length inside the model, which was used to quantitively assess the wound area during procedure. A digital camera (DC-FZ80, Panasonic, Osaka, Japan) and two USB cameras were utilized to record the procedure from different angles.

2.8. Statistical analysis

All quantitative values in this work were reported as means ± standard deviation (SD) with $n = 3$ samples per group.

3. Result and discussion

3.1. Mechanism of embedded printing of engineered lung cancer model

Embedded printing is an emerging extrusion-based 3D printing strategy, in which liquid ink material is extruded through a dispensing nozzle moving in a yield-stress fluid. The fluid can switch its status based on externally applied shear stress. When the nozzle-induced shear stress exceeds the critical yield stress, the fluid presents a liquid state, allowing the nozzle movement to print a 3D structure from the ink in a layer-by-layer manner [27, 28]. When the nozzle moves away, the localized shear stress decreases below the yield stress, making the fluid behave solid-like to stably hold the structure in place until a crosslinking step is performed to either solidify the fluid as a matrix [29, 30] or the structure [31, 32] or both [33, 34]. Because of the excellent supporting capability of the matrix, embedded printing has been extensively utilized to fabricate diverse devices, such as scaffolds [28, 35], organ/tissue equivalents [32, 36], microfluidic chips [30, 37], for a variety of biomedical applications.

In this work, embedded printing is selected as the tool to fabricate a patient-specific lung cancer analogous model. The schematic is summarized in figure 1. Before printing, a CT scanner is applied to collect the geometrical data of the lung and tumor in a patient's

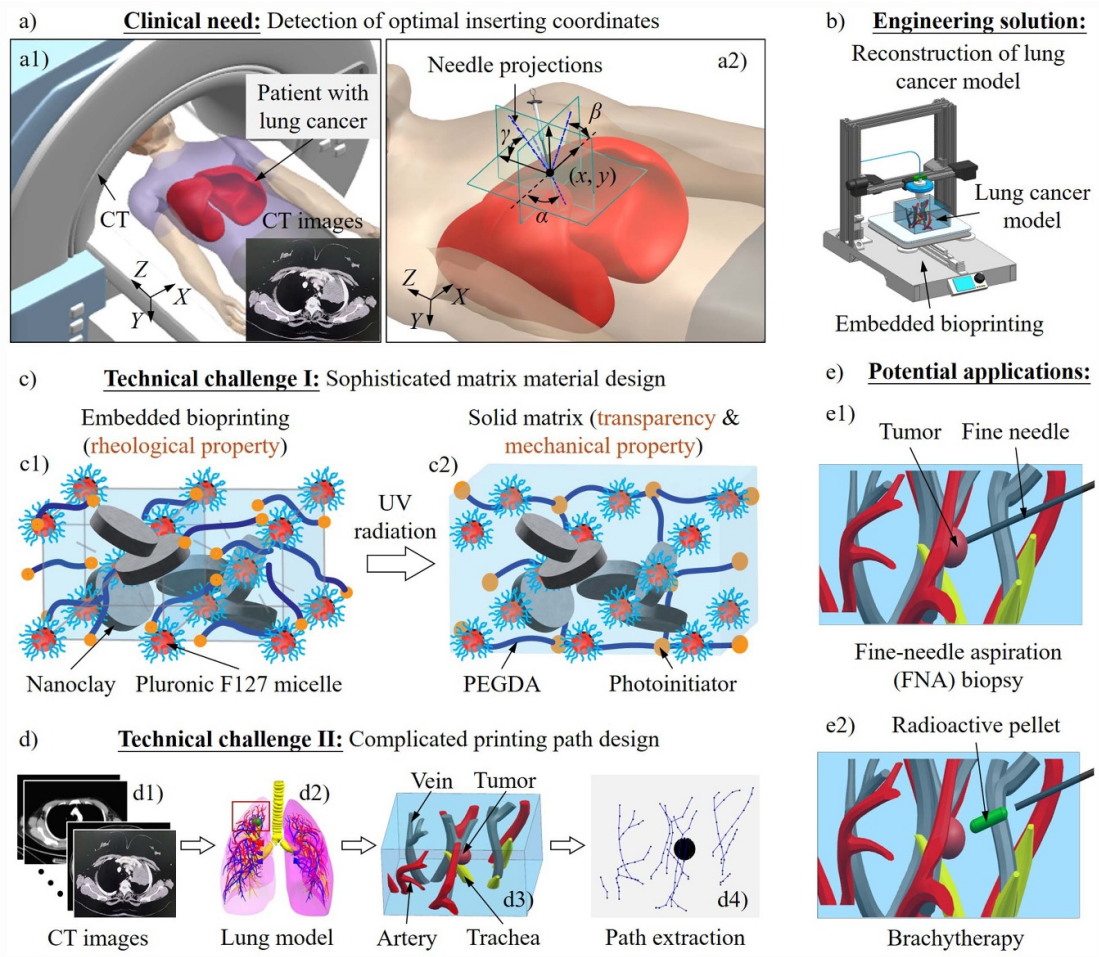

Figure 1. Embedded 3D printing of lung cancer analogous model. (a) Clinical need: (a1) CT imaging of lung and tumor in a patient's body and (a2) resulting virtual 3D model for procedure planning. (b) Engineering solution: reconstruction of lung cancer model for pre-procedure training and detection of optimal inserting coordinates. Two major technical challenges in embedded printing: (c) sophisticated matrix material design and (d) complicated printing path design. (e) Potential applications of the lung cancer model: (e1) FNA biopsy and (e2) brachytherapy.

body, as shown in figure 1(a1). A 3D model can be generated based on the CT images for planning the procedure virtually. Although this model provides an overarching picture of the tumor in the patient's lung, it is still challenging to quantitatively and accurately determine the optimal inserting coordinates for FNA biopsy (figure 1(a2)). Additionally, interventionalists cannot receive hands-on training through this virtual model. With the help of embedded printing, it is technically feasible to convert the virtual model into a practical model by reconstruction of the complicated respiratory track-blood vessel-tumor system within a matrix, as illustrated in figure 1(b).

To fabricate the system, two major engineering challenges need to be tackled. The first challenge is the design of matrix material to fulfill three fundamental requirements, including: (1) suitable rheological properties for embedded printing diverse branched vessels, (2) acceptable transparency before and after crosslinking for better observation of FNA, and (3) mechanical properties similar to those of human tissues for hands-on training purpose, as shown in figure 1(c). Herein, a nanocomposite is developed to function as the matrix for embedded printing, which is composed of four compositions: nanoclay, Pluronic F127, PEGDA, and photoinitiator. Specifically, nanoclay is a classic yield-stress additive with positive charges on the edge and negative charges on faces [38, 39]. When dispersed in an aqueous solvent, electrostatic interactions between nanoclay particles result in the formation of a given microstructure, called a 'house-of-cards' arrangement. Moreover, this chargeability enables nanoclay to be miscible with diverse hydrogels to generate even more complicated microstructures through different mechanisms [40–42]. Thus, higher stress is needed to disrupt the formed microstructure, which not only makes the nanoclay and/or nanoclay-hydrogel system possess a yield-stress property [43] but also enhances the mechanical stiffness of the system. Thus, the main purpose of involving nanoclay in the matrix is to tune the rheological and mechanical properties. Pluronic F127 is a thermosensitive hydrogel composed of a central hydrophobic block

of polypropylene oxide (PPO) flanked by two hydrophilic blocks of polyethylene oxide (PEO). At room temperature and/or higher concentration [44, 45], the PPO blocks aggregate to form a core while the PEO blocks extend outward to generate a corona around the core, leading to the formation of a micelle, as shown in figure 1(c1). Numerous micelles aggregate together to create a jammed microstructure, which integrates with the 'house-of-cards' arrangement from nanoclay to further tune the rheological properties [40, 46]. Moreover, the previous studies demonstrate that nanoclay-Pluronic F127 nanocomposites exhibit a good flowability at low temperatures to facilitate the easy perfusion of matrix into a container without bubbles [40, 46]. In addition, it is found that Pluronic F127 may also affect the transparency when mixing with other materials [47, 48]. Therefore, the major functions of Pluronic F127 in the matrix include the enhancement of rheological properties and adjustment of transparency. PEGDA is a photocurable hydrogel, which serves as the crosslinkable component in the matrix. With the help of photoinitiator, a 3D networked microstructure is formed from PEGDA polymer chains under UV radiation, converting the matrix from a yield-stress fluid to a soft solid (as shown in figure 1(c2)). However, it is observed that the transparency deteriorates in this phase transition. Therefore, it is feasible to adjust the transparency and mechanical properties by changing the concentrations of PEGDA and photoinitiator.

The second challenge is the design and optimization of complicated printing paths (figure 1(d)). Based on the CT images (figure 1(d1)), a virtual lung model can be created which consists of numerous veins, arteries, and tracheae (figure 1(d2)). As illustrated in figure 1(d3), a tumor surrounded by multiple aforementioned vessels yields a complex system in the selected region with limited size. Although the traditional layer-by-layer strategy can simplify the generation of printing paths, the ink deposition in the matrix has to be intermittently ceased as the nozzle moves between different vessels in one layer, which significantly decreases the fabrication efficiency. To quickly reconstruct such a complicated system, a vessel-by-vessel strategy is proposed in this work, which faces two key issues in the path planning stage: (1) it is necessary to extract the spatial coordinates of each vessel and tumor; and (2) an optimization step is needed to determine the printing sequence of all components, aiming to prevent any undesired interference between components, as shown in figure 1(d4). Therefore, a new path planning algorithm must be explored to customize trajectories for the reconstruction of this patient-specific lung cancer model. The engineered model not only benefits the FNA biopsy by providing optimal inserting coordinates (figure 1(e1)) but is also expandable to facilitate other lung cancer treatments, e.g. brachytherapy [49] (figure 1(e2)), offering a reliable technical solution for enhancing lung cancer diagnosis and therapy.

3.2. Design of yield-stress matrix material

Because of the coupling effects of four compositions in the proposed nanocomposite, the orthogonal experiments are designed and conducted to evaluate the role of each composition in tuning rheological properties, transparency, and mechanical properties, as shown in figure 2(a). First, yield stress is selected as the core rheological parameter to quantify the nanocomposite serving as a matrix. The yield stress values are measured in figure S1. By changing the matrix formulas, the nanocomposites present a large variation of yield stress. Particularly, the nanocomposite 1N10F10P0.2I with 1% nanoclay, 10% Pluronic F127, 10% PEGDA, and 0.2% photoinitiator does not have a yield-stress behavior. This is because both the nanoclay and Pluronic F127 concentrations are below their thresholds (∼3% for nanoclay [50] and ∼20% for Pluronic F127 [51]) to form neither 'house-of-cards' arrangement nor jammed microstructure within the nanocomposite. In contrast, the nanocomposite 3N20F20P0.2I has higher concentrations of nanoclay and Pluronic F127, which drive the formation of dual microstructure. One is made of jammed micelles of Pluronic F127 with PPO core surround by PEO corona. The other is the 'house-of-cards' arrangement from nanoclay. These two microstructures coexist in either face-centered cubic or body-centered cubic configuration [40, 44]. Besides, neutral PEGDA molecules may penetrate through the 'house-of-cards' arrangement and have interactions with PEO blocks due to their similar chemical structures, as both are hydrophilic polymers composed of repeating ethylene oxide units. This structural similarity facilitates favorable interactions between PEO blocks of Pluronic F127 and PEGDA chains based on the literature [52, 53]. The complicated microstructure of the nanocomposite results in a high yield stress of over 200 Pa [40, 46]. Based on the orthogonal experiments, the coupling effects of four compositions on yield stress are further analyzed per the protocol in the previously published article [54]. The results are calculated in table S1 and illustrated in figure 2(b). It is observed that although all compositions affect the rheological properties, the change of nanoclay and Pluronic F127 concentration results in the most significant variations of yield stress, which indicates that it is more efficient to tune the rheology by adjusting these two compositions. The range analysis also supports this conclusion. As shown in table S1, the difference values (δ) of nanoclay and Pluronic F127 are 100.79 and 66.77, respectively, much higher than those of PEGDA and photoinitiator (∼40). Therefore, if high yield stress is targeted,

a)

Orthogonal experimental design

Expt. No.	Factors: Photo-initiator	Nanoclay	Pluronic F127	PEGDA
1	0.2%	1%	10%	10%
2	0.2%	2%	15%	15%
3	0.2%	3%	20%	20%
4	0.5%	1%	15%	20%
5	0.5%	2%	20%	10%
6	0.5%	3%	10%	15%
7	0.8%	1%	20%	15%
8	0.8%	2%	10%	20%
9	0.8%	3%	15%	10%

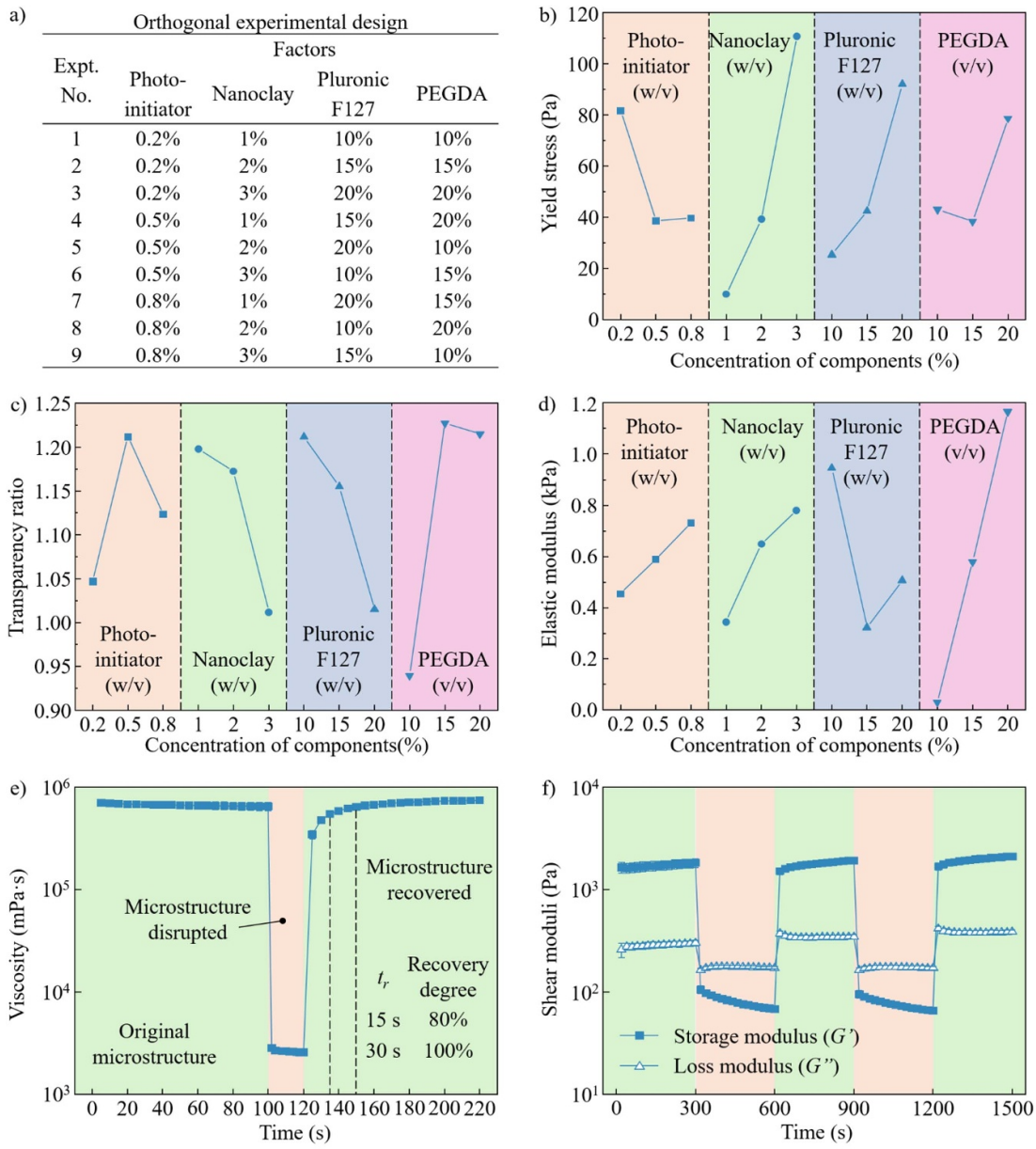

Figure 2. Design of yield-stress matrix material. (a) Orthogonal experimental design. Evaluation of the coupling effects of nanoclay, Pluronic F127, PEGDA, and photoinitiator on (b) yield stress, (c) transparency ratio, and (d) elastic modulus. (e) Recovery time of the nanocomposite after shearing. (f) Repeatability of the nanocomposite during alternatively shearing.

it is necessary to increase the concentration of nanoclay and Pluronic F127.

After that, the matrix's transparency after UV crosslinking is quantified by using the transparency ratio of 1.0 as the criterion, which is defined as the ratio of matrix transparency to the transparency of a Petri dish. The results are summarized in figure S2. The nanocomposite 1N15F20P0.5I has a ratio of around 1.4, much higher than the target ratio of 1.0, which indicates that this nanocomposite presents a poor transparency as demonstrated in the inset of figure S2. In contrast, some nanocomposites, e.g. 1N10F10P0.2I and 2N20F10P0.5I, possess ratios close to 1.0. Their transparencies are acceptable based on the inset of figure S2. The range analysis results are shown in figure 2(c) and table S2. Among the four compositions of the matrix material, PEGDA has the most significant effect on the transparency with the highest δ value. With the increase of PEGDA concentration, the transparency of nanocomposite deteriorates. However, both nanoclay and Pluronic F127 have positive effects on the improvement of transparency. As shown in figure 2(c), when the nanoclay and Pluronic F127 concentrations increase from 1%–3% and 10%–20%, respectively, the transparency ratio decreases from around 1.2 to 1.0. This may be because the existence of more nanoclay particles and Pluronic F127 micelles enlarge the 3D networked microstructure formed by PEGDA polymer chains, making visible light easily penetrate through the crosslinked nanocomposite to finally enhance the transparency [55, 56]. Therefore, by controlling the concentration

of nanoclay and Pluronic F127, it is technically feasible to gain the nanocomposite with acceptable transparency even at a higher PEGDA concentration.

Finally, the elastic modulus is selected to assess the coupling effects of the compositions on the mechanical properties. The measurements are summarized in figure S3. Different from the brittle nature of crosslinked PEGDA with a low molecular weight, all nanocomposites exhibit better flexibility. This may be attributed to the interactions between PEGDA molecules and PEO blocks of Pluronic F127, resulting in the plasticizing effects to enhance the extensibility and softness of the crosslinked material, as reported in the published studies [52, 57, 58]. Based on the measurements, the nanocomposites present a variety of elastic modulus ranging from 0.09 to 1.72 kPa with the change of the formula. Particularly, the nanocomposite 2N10F20P0.8I has the maximum elastic modulus which is composed of the highest concentration of PEGDA. Based on the range analysis in figure 2(d) and table S3, the nanocomposite's mechanical properties are more sensitive to PEGDA: when its concentration increases from 10% to 20%, the elastic modulus increases from almost 0 to around 1.2 kPa. This is because more PEGDA polymer chains in the crosslinked nanocomposite can densify the formed 3D networked microstructure, enhancing the mechanical stiffness of the matrix at the macroscale. By comprehensively evaluating the role of each composition, the nanocomposite 3N20F20P0.2I is determined as the optimal matrix in the orthogonal experimental design for 3D printing the lung cancer model, which has a yield stress value of 203.16 Pa, falling in the desired range of 100–500 Pa [27, 40, 43, 46], acceptable transparency (0.91), and elastic modulus (1.13 kPa) close to that of lung tissues (1–5 kPa) [59].

The functionality of the optimal nanocomposite as a matrix is further characterized by rheological measurements. On one hand, the recovery time is quantified by shearing the nanocomposite at a higher stress to disrupt its microstructure and then decreasing the shear stress, as shown in figure 2(e). It takes around 15 s for the nanocomposite to recover 80% of the microstructure and 30 s to be fully recovered. This recovery time is comparable with the published results [60–62], which validates the potential of the nanocomposite for embedded printing purposes. On the other hand, the nanocomposite experiences alternatively shearing at low and high strains to mimic the repeated nozzle movement in a matrix bath. As shown in figure 2(f), the storage modulus (G') is higher than the loss modulus (G'') at a lower strain, which demonstrates the nanocomposite behaves like a solid. When the strain is increased to a higher level, G'' exceeds G', showing a solid-to-liquid transition. The measured shear moduli in multiple cycles are consistent, which proves the good repeatability of the nanocomposite.

3.3. Design of printing path

Because multiple components (veins, arteries, tracheae, and tumor) coexist in the selected lung area, conventional layer-by-layer strategy cannot effectively generate printing paths for such a complicated system. In this work, a new path generation platform is proposed and developed, as shown in figure 3(a). First, a 3D model is generated based on the CT images. Each component is distinguished in the model. Then, one component is imported into a commercial software Grasshopper to generate the lattice. The print track of this component is extracted according to the lattice. After collecting the print tracks of all components, their coordinates are exported to determine the edge validity using the algorithm in figure S4. The purpose is to evaluate whether adjacent components conflict with each other or not. One example is illustrated in figure 3(b1). When depositing a vein and a tumor in the matrix, the tumor needs to be printed first because the nozzle may conflict with the vein if it is previously created in the matrix. Another example is the printing of a trachea and vein. As shown in figure 3(b2), the branch of the vein has an edge conflict with the trachea. As a result, the trachea must be printed first to prevent the interference. Finally, using the validity results, the printing path is generated through the algorithm in figure S5. Specifically, the selected area of the lung cancer model is composed of 5 veins, 4 arteries, 3 tracheae, and 1 tumor. The printing sequence of these components is summarized in figure 3(c).

3.4. Determination of printing parameters

In this work, an epoxy-based ink is used to print all the components in the matrix bath. It is noted that the pure epoxy solution exhibits significantly low viscosity, which has a poor printability and shape fidelity for 3D printing [46, 63]. To address these issues, fumed silica is incorporated and mixed with the epoxy, transforming it from a shear-thinning liquid into a yield-stress fluid, as shown in figure S6. Although the diameter of an extruded filament is affected by many parameters (such as nozzle size and dispensing pressure), path speed is the most practical way to continuously adjust the filament geometry during printing. After summarizing the truck and branch sizes of the veins, arteries, and tracheae in table S4, the path speed is varied in a large range to filter the candidate speeds for embedded printing the filaments with target diameters, as shown in figure S7. Then, the path speeds are refined to make the filament diameters close to the size range of veins, arteries, and tracheae, as illustrated in figure 3(d). For tumor printing, the extrusion time is applied to control the diameter of the deposited spheroid. As shown in figure 3(e), the dispensing nozzle is moved to the pre-defined location, inserted into the matrix bath, and starts to extrude the epoxy-based ink. With the increase of the extrusion

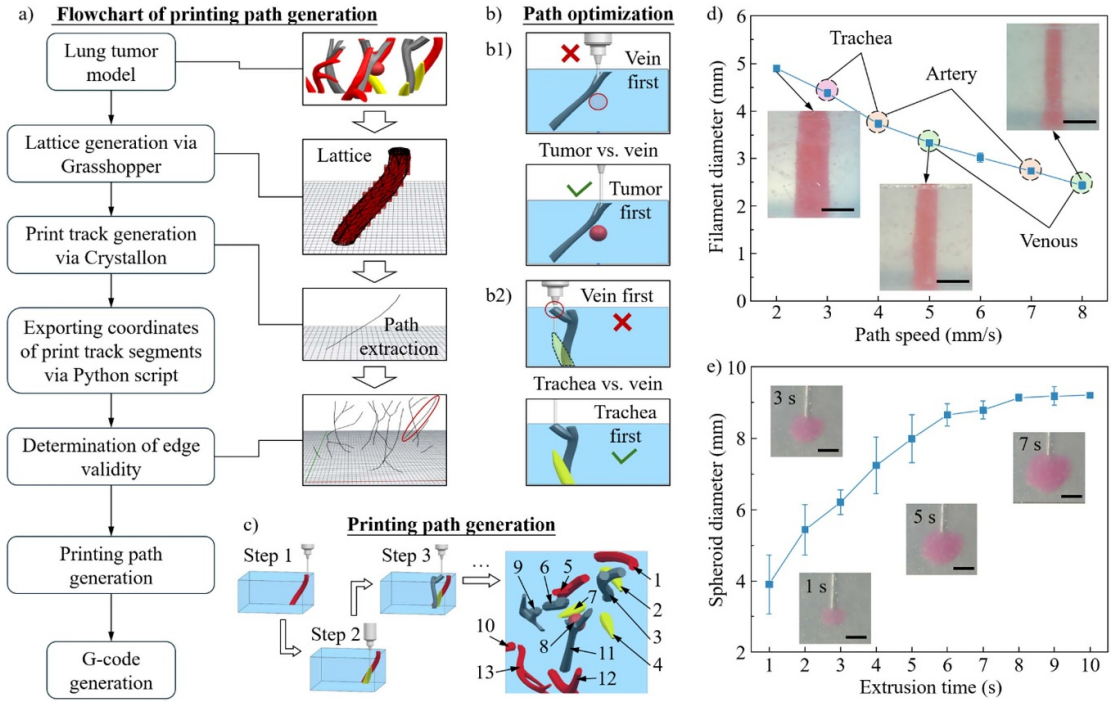

Figure 3. Design of printing path and determination of printing parameters. (a) New platform to generate printing path for the multi-component system. (b) Two path optimization cases in lung cancer model printing: (b1) tumor vs. vein, and (b2) trachea vs. vein. (c) Generated printing path for reconstructing the target lung cancer model. (d) Filament diameter as a function of path speed. (e) Spheroid diameter as a function of extrusion time. Scale bars: 5.0 mm.

time, the spheroid diameter increases from around 4–9 mm.

3.5. Embedded printing of lung cancer model and FNA biopsy demonstration

Based on the designed virtual model (figure 4(a1)) and optimized printing paths, a 3D lung cancer model is successfully printed within the matrix bath, as shown in figure 4(a2) and movie S1. Because the epoxy-based ink is hydrophobic while the nanocomposite is composed of many hydrophilic compositions, interfacial tension exists between ink filament and matrix, which serves as a barrier to effectively prevent the diffusion-induced filament swelling, as shown in figure S8a. In addition, due to the high yield stress of the nanocomposite, each deposited component is stabilized *in situ* during printing. Filaments demonstrate negligible shrinkage, as validated in figure S8(b). Furthermore, the acceptable transparency of the matrix enables the observation of all components. Specifically, the tumor analogue is clearly detected in the model (figure 4(a2)). After printing, UV radiation is applied to chemically crosslink the matrix and entrap the components, as illustrated in figure 4(a3). Movie S2 also records this process. After treatments, the engineered lung cancer model (figure 4(a4)) is achieved which can be released from the container for FNA biopsy planning purposes. The similarity between the designed model and the printed one was quantitatively assessed in figure S9 with the SSIM of around 79.92%, indicating a high level of accuracy.

To demonstrate the functionality of the printed model, two datum planes (*XZ* and *YZ* in figure 4(b1)) are established first to receive the projections of a fine needle at different angles. The needle can be inserted into the engineered lung cancer model from different locations and directions (x_i, y_i, α_i, β_i, γ_i), as shown in the schematic in figure 4(b2). The optimal procedure plan can be determined by comprehensively evaluating the insertion depth (d_i in figure 4(b3)) as well as examining the potential interferences with veins, arteries, and tracheae. In this work, five points are selected on the surface of the matrix based on the observation, which are used as the candidate inserting locations. As illustrated in figure 4(c), the center of the model is set as the origin and the coordinates of each point are measured accordingly and summarized in table S5. At each location, the fine needle is inserted towards the tumor analogue within the matrix, as shown in figure 4(d1). The angles of the needle in *XY*, *XZ*, and *YZ* planes are measured in the top (figure 4(d2)), front (figure 4(d3)), and side views (figure 4(d4)), respectively, which can be used as the directional information to guide the FNA biopsy. The process is recorded in movie S3.

The insertion depth at each location is measured and the results are summarized in figure 4(e). At Positions 1 and 2, the fine needle can reach the tumor analogue with the insertion depths approaching 20 mm. Position 3 has a minimum insertion depth

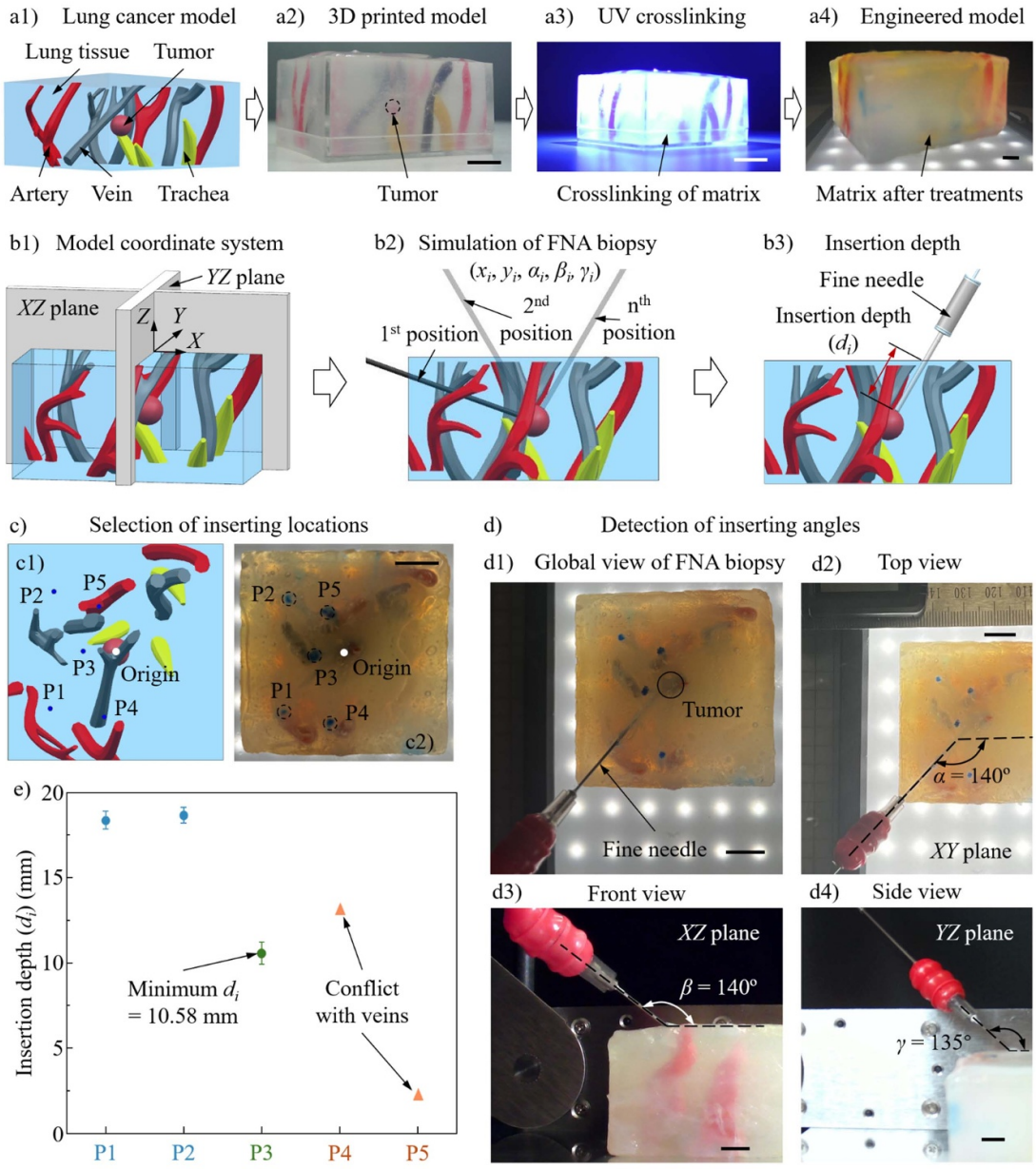

Figure 4. Embedded printing of lung cancer model and FNA biopsy demonstration. (a) Key steps in lung cancer model printing. (b) Schematic of FNA biopsy planning. (c) Selection of inserting locations on the model surface. (d) Collection of inserting directions using the model. (e) Evaluation of the FNA procedure plans. Scale bars: 10 mm.

of 10.58 mm. In addition, the fine needle does not interfere with veins, arteries, or tracheae during insertion. At Positions 4 and 5, the fine needle is inserted into the veins within the engineered model, which indicates that these two locations are not suitable for FNA biopsy. Thus, Position 3 is one of the optimal choices which not only prevents any needle-vessel conflicts but also offers the shortest insertion depth to minimize the wound area. The directional information (α_3, β_3, γ_3) at Position 3 can be provided to interventionalists to guide the procedure.

3.6. Discussion

In this study, the new path design strategy enables the construction of veins, arteries, and tracheae within the model in a vessel-by-vessel manner, which is more efficient than the current layer-by-layer printing manner, especially when creating scaled-up vascular architectures. The path generation platform is therefore promising to plan and optimize printing paths for the biofabrication of diverse tissues and organs in the future. Additionally, the coupling effects of multiple components (i.e. nanoclay, Pluronic F127, and PEGDA) on the rheological and mechanical properties as well as transparency are comprehensively evaluated, which can guide the design of yield-stress nanocomposites for different embedded printing purposes.

Although the engineered lung cancer model demonstrates the feasibility of guiding the FNA

biopsy procedure, some concerns still remain that need to be further investigated. First, the matrix bath's transparency is acceptable in this work to observe the fine-needle inserting process as well as detect the interferences between the needle and the printed veins, arteries, and tracheae, as shown in movie S3. A high-molecular-weight PEGDA can be used to prepare the matrix, if an improved transparency is required, which has been reported as an effective way to enhance the transparency of hydrogel or composite after UV crosslinking [64, 65]. Second, elastic modulus of the matrix is selected as the indicator to evaluate the mechanical properties, which may not be sufficient. More biomechanical properties, such as ultimate tensile strength, plasticity, stiffness [66, 67], etc will be considered in the future, which are expected to comprehensively assess the functionality of the engineered model in accurately mimicking human lung tissues. Third, although the vessel-by-vessel manner shortens the printing time to around 1 min (movie S1), the long-term crosslinking of the commercial epoxy extends the fabrication cycle to around 24 h. Fast crosslinking materials can be used as inks in the future studies, if a high fabrication efficiency is the target. Fourth, one major limitation of the embedded printing strategy developed in this work is the shape diversity of the lung model. Because the printing process is embedded within a container, the overall shape of the model is constrained by the container's shape, which is far away from a real human lung. The advancements of other 3D printing strategies, such as sequential printing in a reversible ink template [68], hybrid direct ink writing/embedded 3D printing [69], and inverse embedded 3D printing [63, 70], can be integrated with the strategy in this study to produce anatomic-level lung cancer models, even with skins and muscles, for clinical FNA biopsy training. Finally, since the purpose of the model is for FNA biopsy training, living cells are not used in the printing process. In the future, cellular models (with both normal and tumor cells) will be printed using the same strategy by replacing PEGDA and epoxy-based ink with more biocompatible materials, which can be used for brachytherapy.

4. Conclusion and future work

In this study, an embedded 3D printing strategy is developed and utilized to reconstruct a patient-specific lung tumor model. The coupling effects of different compositions in the nanocomposite on its rheological property, transparency, and mechanical property, are systematically investigated. In addition, a new platform is established to generate printing paths in a multi-component system. To prove the effectiveness of the 3D printing strategy, a lung tumor model composed of veins, arteries, tracheae, and tumor is successfully printed, which can predict the optimal inserting location and direction for planning FNA procedure.

To reduce the fabrication time, only a portion of the lung cancer model is selected and reconstructed. A full-scale human lung cancer model will be printed in the future which can provide more accurate information for procedure planning. Also, in this work, only one spherical tumor is integrated with the healthy lung to make the lung cancer model. From the clinical perspective, tumors may exist randomly in a patient's lung with irregular shapes. More sophisticated path planning algorithms will be explored in the future that can assist in the fabrication of high-precision lung cancer models, which are promising to guide the clinic FNA biopsy in the future.

Data availability statement

All data that support the findings of this study are included within the article (and any supplementary files).

Acknowledgment

W H and C Z contributed equally to this work. W H, C Z, Y Y, D Z, N X, and Y J designed research; W H, C Z, L R, K M, K X, R C, E B, and M B performed research; W H and C Z analyzed data; Y Y, D Z, N X, and Y J supervised project; and W H, C Z, L R, Y Y, D Z, N X, and Y J wrote the paper. L R would like to acknowledge the support of the National Science Foundation Graduate Research Fellowship Program through NSHE sub-award number: AWD0002282-1937966. R C would like to acknowledge the support of the National Science Foundation Graduate Research Fellowship Program through NSHE sub-award number: AWD01-00002282. D Z acknowledges the support of the National Key R&D Program of China (2018YFA0703000) and the National Natural Science Foundation of China (52175289). Y J acknowledges the support of the National Science Foundation (OIA-2229004).

ORCID iDs

Manish Bishwokarma https://orcid.org/0009-0002-6700-8886
Yifei Jin https://orcid.org/0000-0003-4336-1802

References

[1] Kratzer T B, Bandi P, Freedman N D, Smith R A, Travis W D, Jemal A and Siegel R L 2024 Lung cancer statistics, 2023 *Cancer* **130** 1330–48
[2] Tavares-Negrete J A, Das P, Najafikhoshnoo S, Zanganeh S and Esfandyarpour R 2023 Recent advances in lung-on-a-chip technology for modeling respiratory disease *Bio-des. Manuf.* **6** 563–85
[3] Dwyer L L, Vadagam P, Vanderpoel J, Cohen C, Lewing B and Tkacz J 2024 Disparities in lung cancer: a targeted

literature review examining lung cancer screening, diagnosis, treatment, and survival outcomes in the United States *J. Racial. Ethn. Health Disp.* **11** 1489–500
[4] Woolf C R 1954 Applications of aspiration lung biopsy with a review of the literature *Dis. Chest* **25** 286–301
[5] Heerink W J, de Bock G H, de Jonge G J, Groen H J, Vliegenthart R and Oudkerk M 2017 Complication rates of CT-guided transthoracic lung biopsy: meta-analysis *Eur. Radiol.* **27** 138–48
[6] Raj R, Raparia K, Lynch D A and Brown K K 2017 Surgical lung biopsy for interstitial lung diseases *Chest* **151** 1131–40
[7] Amedee R G and Dhurandhar N R 2001 Fine-needle aspiration biopsy *Laryngoscope* **111** 1551–7
[8] Gharib H and Goellner J R 1993 Fine-needle aspiration biopsy of the thyroid: an appraisal *Ann. Intern. Med.* **118** 282–9
[9] Nadda R, Sahani A K and Repaka R 2022 A systematic review of real-time fine-needle aspiration biopsy methods for soft tissues *IETE Tech. Rev.* **39** 1011–26
[10] Sachdeva M, Ronaghi R, Mills P K and Peterson M W 2016 Complications and yield of computed tomography-guided transthoracic core needle biopsy of lung nodules at a high-volume academic center in an endemic coccidioidomycosis area *Lung* **194** 379–85
[11] Colella S, Scarlata S, Bonifazi M, Ravaglia C, Naur T M, Pela R, Clementsen P F, Gasparini S and Poletti V 2018 Biopsy needles for mediastinal lymph node sampling by endosonography: current knowledge and future perspectives *J. Thoracic Dis.* **10** 6960
[12] Sung S, Crapanzano J P, DiBardino D, Swinarski D, Bulman W A and Saqi A 2018 Molecular testing on endobronchial ultrasound (EBUS) fine needle aspirates (FNA): impact of triage *Diagn. Cytopathol.* **46** 122–30
[13] Nassar A 2011 Core needle biopsy versus fine needle aspiration biopsy in breast—a historical perspective and opportunities in the modern era *Diagn. Cytopathol.* **39** 380–8
[14] Conti C B, Cereatti F and Grassia R 2019 Endoscopic ultrasound-guided sampling of solid pancreatic masses: the fine needle aspiration or fine needle biopsy dilemma. Is the best needle yet to come? *World J. Gastrointest. Endosc.* **11** 454
[15] Santoni S, Gugliandolo S G, Sponchioni M, Moscatelli D and Colosimo B M 2022 3D bioprinting: current status and trends—a guide to the literature and industrial practice *Bio-des. Manuf.* **5** 14–42
[16] Guillemot F, Mironov V and Nakamura M 2010 Bioprinting is coming of age: report from the International Conference on Bioprinting and Biofabrication in Bordeaux (3B'09) *Biofabrication* **2** 010201
[17] Handral H K, Natu V P, Cao T, Fuh J Y, Sriram G and Lu W F 2022 Emerging trends and prospects of electroconductive bioinks for cell-laden and functional 3D bioprinting *Bio-des. Manuf.* **5** 396–411
[18] Wu W, Liu S, Wang L, Wu B, Zhao L, Jiang W, Dai K, Hao Y, Fu L and Ai S 2022 Application of 3D printing individualized guide plates in percutaneous needle biopsy of acetabular tumors *Front. Genet.* **13** 955643
[19] Zhang X, Yang D, Li L, Wang J, Liang S, Li P, Han Z, Wang X and Zhang K 2024 Application of three-dimensional technology in video-assisted thoracoscopic surgery sublobectomy *Front. Oncol.* **14** 1280075
[20] She C *et al* 2024 Noninvasive targeting system with three-dimensionally printed customized device in stereotactic brain biopsy *World Neurosurg.* **183** e649–e57
[21] Mei Y, Wu D, Berg J, Tolksdorf B, Roehrs V, Kurreck A, Hiller T and Kurreck J 2023 Generation of a perfusable 3D lung cancer model by digital light processing *Int. J. Mol. Sci.* **24** 6071
[22] Herreros-Pomares A, Zhou X, Calabuig-Fariñas S, Lee S J, Torres S, Esworthy T, Hann S Y, Jantus-Lewintre E, Camps C and Zhang L G 2021 3D printing novel *in vitro* cancer cell culture model systems for lung cancer stem cell study *Mater. Sci. Eng.* C **122** 111914
[23] Liu X, Zhao Y, Xuan Y, Lan X, Zhao J, Lan X, Han B and Jiao W 2019 Three-dimensional printing in the preoperative planning of thoracoscopic pulmonary segmentectomy *Transl. Lung Cancer Res.* **8** 929
[24] Yoon S H, Park S, Kang C H, Park I K, Goo J M and Kim Y T 2019 Personalized 3D-printed model for informed consent for stage I lung cancer: a randomized pilot trial *Semin. Thoracic Cardiovasc. Surg.* **31** 316–8
[25] Baba M *et al* 2017 Development of a tailored thyroid gland phantom for fine-needle aspiration cytology by three-dimensional printing *J. Surg. Educ.* **74** 1039–46
[26] Zhu H, Kim Y D and De Kee D 2005 Non-Newtonian fluids with a yield stress *J. Non-Newton. Fluid Mech.* **129** 177–81
[27] Hua W, Mitchell K, Raymond L, Godina B, Zhao D, Zhou W and Jin Y 2021 Fluid bath-assisted 3D printing for biomedical applications: from pre- to postprinting stages *ACS Biomater. Sci. Eng.* **7** 4736–56
[28] Tarafder S, Koch A, Jun Y, Chou C, Awadallah M R and Lee C H 2016 Micro-precise spatiotemporal delivery system embedded in 3D printing for complex tissue regeneration *Biofabrication* **8** 025003
[29] Weisgrab G, Ovsianikov A and Costa P F 2019 Functional 3D printing for microfluidic chips *Adv. Mater. Technol.* **4** 1900275
[30] Hua W, Mitchell K, Raymond L, Valentin N, Coulter R and Jin Y 2023 Embedded 3D printing of PDMS-based microfluidic chips for biomedical applications *J. Manuf. Sci. Eng.* **145** 011002
[31] Bhattacharjee T, Zehnder S M, Rowe K G, Jain S, Nixon R M, Sawyer W G and Angelini T E 2015 Writing in the granular gel medium *Sci. Adv.* **1** e1500655
[32] Shiwarski D J, Hudson A R, Tashman J W and Feinberg A W 2021 Emergence of FRESH 3D printing as a platform for advanced tissue biofabrication *APL Bioeng.* **5** 010904
[33] Bas J, Dutta T, Llamas Garro I, Velázquez-González J S, Dubey R and Mishra S K 2024 RETRACTED: embedded sensors with 3D printing technology: review *Sensors* **24** 1955
[34] Muth J T, Vogt D M, Truby R L, Mengüç Y, Kolesky D B, Wood R J and Lewis J A 2014 Embedded 3D printing of strain sensors within highly stretchable elastomers *Adv. Mater.* **26** 6307–12
[35] Bilici C, Altunbek M, Afghah F, Tatar A G and Koç B 2023 Embedded 3D printing of cryogel-based scaffolds *ACS Biomater. Sci. Eng.* **9** 5028–38
[36] Mirdamadi E, Tashman J W, Shiwarski D J, Palchesko R N and Feinberg A W 2020 FRESH 3D bioprinting a full-size model of the human heart *ACS Biomater. Sci. Eng.* **6** 6453–9
[37] Alioglu M A, Singh Y P, Nagamine M, Rizvi S H, Pal V, Gerhard E M, Saini S, Kim M H and Ozbolat I T 2023 3D embedded printing of microfluidic devices using a functional silicone composite support bath *Addit. Manuf.* **70** 103566
[38] Gaharwar A K, Cross L M, Peak C W, Gold K, Carrow J K, Brokesh A and Singh K A 2019 2D nanoclay for biomedical applications: regenerative medicine, therapeutic delivery, and additive manufacturing *Adv. Mater.* **31** 1900332
[39] Thompson D W and Butterworth J T 1992 The nature of laponite and its aqueous dispersions *J. Colloid Interface Sci.* **151** 236–43
[40] Hua W, Mitchell K, Kariyawasam L S, Do C, Chen J, Raymond L, Valentin N, Coulter R, Yang Y and Jin Y 2022 Three-dimensional printing in stimuli-responsive yield-stress fluid with an interactive dual microstructure *ACS Appl. Mater. Interfaces* **14** 39420–31
[41] Dávila J L and d'Ávila M A 2019 Rheological evaluation of laponite/alginate inks for 3D extrusion-based printing *Int. J. Adv. Manuf. Technol.* **101** 675–86
[42] Li Z, Li C, Sun W, Bai Y, Li Z and Deng Y 2023 A controlled biodegradable triboelectric nanogenerator based on PEGDA/laponite hydrogels *ACS Appl. Mater. Interfaces* **15** 12787–96
[43] Wu Q, Song K, Zhang D, Ren B, Sole-Gras M, Huang Y and Yin J 2022 Embedded extrusion printing in yield-stress-fluid baths *Matter* **5** 3775–806

[44] Pozzo D C and Walker L M 2007 Small-angle neutron scattering of silica nanoparticles templated in PEO–PPO–PEO cubic crystals *Colloids Surf.* A **294** 117–29
[45] Mortensen K, Batsberg W and Hvidt S 2008 Effects of PEO−PPO diblock impurities on the cubic structure of aqueous PEO−PPO−PEO pluronics micelles: fcc and bcc ordered structures in F127 *Macromolecules* **41** 1720–7
[46] Zhang C *et al* 2024 Multiscale embedded printing of engineered human tissue and organ equivalents *Proc. Natl Acad. Sci.* **121** e2313464121
[47] Plisko T V, Penkova A V, Burts K S, Bildyukevich A V, Dmitrenko M E, Melnikova G B, Atta R R, Mazur A S, Zolotarev A A and Missyul A B 2019 Effect of Pluronic F127 on porous and dense membrane structure formation via non-solvent induced and evaporation induced phase separation *J. Membr. Sci.* **580** 336–49
[48] Melosh N A, Lipic P, Bates F S, Wudl F, Stucky G D, Fredrickson G H and Chmelka B F 1999 Molecular and mesoscopic structures of transparent block copolymer−silica monoliths *Macromolecules* **32** 4332–42
[49] Yoon S M *et al* 2021 Outcomes with multi-disciplinary management of central lung tumors with CT-guided percutaneous high dose rate brachyablation *Radiat. Oncol.* **16** 99
[50] Willenbacher N 1996 Unusual thixotropic properties of aqueous dispersions of laponite RD *J. Colloid Interface Sci.* **182** 501–10
[51] da Silva L C, Borges A C, de Oliveira M G and de Farias M A 2020 Visualization of supramolecular structure of Pluronic F127 micellar hydrogels using cryo-TEM *MethodsX* **7** 101084
[52] Li Q, Ma L, Gao Z, Yin J, Liu P, Yang H, Shen L and Zhou H 2022 Regulable supporting baths for embedded printing of soft biomaterials with variable stiffness *ACS Appl. Mater. Interfaces* **14** 41695–711
[53] Singh K, Wychowaniec J K, Edwards-Gayle C J, Reynaud E G, Rodriguez B J and Brougham D F 2024 Structure-dynamics correlations in composite PF127-PEG-based hydrogels; cohesive/hydrophobic interactions determine phase and rheology and identify the role of micelle concentration in controlling 3D extrusion printability *J. Colloid Interface Sci.* **660** 302–13
[54] Mitchell K, Urade S, Kershaw A, Chu P and Jin Y 2023 3D printing of conical centrifuge system for mineral particle separation *Sep. Purif. Technol.* **306** 122567
[55] Wang C, Zhou B P, Zeng X P, Hong Y Y, Gao Y B and Wen W J 2015 Enhanced photochromic efficiency of transparent and flexible nanocomposite films based on PEO–PPO–PEO and tungstate hybridization *J. Mater. Chem.* C **3** 177–86
[56] Wang Z, Huang C, Han X, Li S, Wang Z, Huang J, Liu H and Chen Z 2022 Fabrication of aerogel scaffolds with adjustable macro/micro-pore structure through 3D printing and sacrificial template method for tissue engineering *Mater. Des.* **217** 110662
[57] Fonseca-García A, Osorio B H, Aguirre-Loredo R Y, Calambas H L and Caicedo C 2022 Miscibility study of thermoplastic starch/polylactic acid blends: thermal and superficial properties *Carbohydr. Polym.* **293** 119744
[58] Li J, Li Y, Lee T C and Huang Q 2013 Structure and physical properties of zein/Pluronic F127 composite films *J. Agric. Food Chem.* **61** 1309–18
[59] Hinz B 2012 Mechanical aspects of lung fibrosis *Proc. Am. Thoracic Soc.* **9** 137–47
[60] Grosskopf A K, Truby R L, Kim H, Perazzo A, Lewis J A and Stone H A 2018 Viscoplastic matrix materials for embedded 3D printing *ACS Appl. Mater. Interfaces* **10** 23353–61
[61] Mahmoudi M, Burlison S R, Moreno S and Minary-Jolandan M 2021 Additive-free and support-free 3D printing of thermosetting polymers with isotropic mechanical properties *ACS Appl. Mater. Interfaces* **13** 5529–38
[62] Wang Y *et al* 2024 Personalized piezoresistive anti-scar orthosis with precise pressure monitoring function based on embedded 3D printing *Adv. Funct. Mater.* **34** 2400208
[63] Hua W, Zhang C, Raymond L, Mitchell K, Wen L, Yang Y and Jin Y 2023 3D printing-based full-scale human brain for diverse applications *Brain*-X **1** e5
[64] Zhang H, Wang L, Song L, Niu G, Cao H, Wang G and Zhu S 2011 Controllable properties and microstructure of hydrogels based on crosslinked poly(ethylene glycol) diacrylates with different molecular weights *J. Appl. Polym. Sci.* **121** 531–40
[65] Pelras T, Glass S, Scherzer T, Elsner C, Schulze A and Abel B 2017 Transparent low molecular weight poly(ethylene glycol) diacrylate-based hydrogels as film media for photoswitchable drugs *Polymers* **9** 639
[66] Tata P R and Rajagopal J 2017 Plasticity in the lung: making and breaking cell identity *Development* **144** 755–66
[67] Park H S, Shin H J, Shin K C, Cha J H, Chae E Y, Choi W J and Kim H H 2018 Comparison of peritumoral stromal tissue stiffness obtained by shear wave elastography between benign and malignant breast lesions *Acta Radiol.* **59** 1168–75
[68] Fang Y, Guo Y, Wu B, Liu Z, Ye M, Xu Y and Xiong Z 2023 Expanding embedded 3D bioprinting capability for engineering complex organs with freeform vascular networks *Adv. Mater.* **35** 2205082
[69] Raymond L, Bandala E, Coulter R, Valentin N, Mitchell K, Hua W and Jin Y 2023 Hybrid direct ink writing/embedded three-dimensional printing of smart hinge from shape memory polymer *Manuf. Lett.* **35** 609–19
[70] Zhao J, Hussain M, Wang M, Li Z and He N 2020 Embedded 3D printing of multi-internal surfaces of hydrogels *Addit. Manuf.* **32** 101097